RSC Applied Interfaces

ROYAL SOCIETY OF CHEMISTRY

PAPER

View Article Online
View Journal | View Issue

Cite this: *RSC Appl. Interfaces*, 2025, **2**, 390

Photocatalytically active metal–organic derived ensembles for organic pollutant degradation†

Clara López-García, Celia Castillo-Blas, ‡ Marta Iglesias, M. Angeles Monge, Enrique Gutiérrez-Puebla * and Felipe Gándara *

Received 27th June 2024,
Accepted 31st July 2024

DOI: 10.1039/d4lf00233d

rsc.li/RSCApplInter

The thermal treatment of metal–organic frameworks (MOFs) incorporating multiple metal elements produces solids with specific features that strongly depend on the parent MOF composition. Thus, metal–organic derived ensembles (MODEs) can be obtained from the pyrolysis process of multi-metal MOFs and can be composed of differently distributed chemical components. In particular, here we show how a series of isoreticular multi-metal MOFs with different combinations of up to four metal elements (Zn, Co, Mn, Ca) subjected to the same thermal process produce complex materials with similar yet distinct composition and distribution of their components. Their characterization using a combination of techniques shows that thermal treatment under a nitrogen atmosphere results in the formation of solids with the presence of metal nanoparticles supported on metal fluoride, which are embedded in a carbonaceous matrix. We prove that they are effective in the photocatalytic degradation of organic pollutants, such as organic dyes or drugs.

Introduction

Metal–organic frameworks (MOFs) are a class of materials built from the combination of metal elements and organic linkers to create periodic structures with potential porosity.[1] Multi-variate (MTV), multi-metal (MM) MOFs incorporate different metal elements in topologically equivalent positions, and they provide a suitable platform for creating materials of increasing complexity by combining different arrangements of metal cations.[2,3] In addition, the thermal treatment of MM-MTV-MOFs is an attractive strategy to obtain other types of complex solids with adjustable activity, for example, to be used as catalysts in reactions that require conditions that are not compatible with the direct use of the MOFs.[4–7] Thus, calcination of multi-metal MOFs results in the formation of multi-metal oxides with various compositions,[8–13] although exerting control over the metal ratios is still challenging. We have already shown that these metal–organic derived oxides might then be used as electrocatalysts in the oxygen reduction reaction,[14] or as pre-catalysts for the reverse water gas shift reaction.[15] Alternatively, pyrolysis of MM-MTV-MOFs typically leads to the formation of hybrid materials, such as carbonaceous species containing metal or metal oxide nanoparticles. Materials obtained through this route have already been employed for several applications,[16–18] including the catalytic degradation of organic pollutants from water.[19–28] Nowadays, the presence of organic pollutants in water represents a relevant societal problem for a number of reasons. Many organic contaminants have been linked to health risks, and exposure to them through water consumption or contact might represent a health issue. Besides, their presence might have a significant impact on the environment and damage aquatic ecosystems, negatively affecting the availability of resources. Moreover, water contamination by organic pollutants results in increased economic costs associated with their removal, or in decreased productivity from water-dependent industries, which negatively affects communities. Therefore, removing pollutants from water has become a major concern and great efforts are being made to develop efficient methods for removing them.

Two classes of the most commonly found organic pollutants are dyes and pharmaceuticals. Removal of organic pollutants might be achieved by different methods, including adsorption, coagulation, filtration, biological treatment, or chemical oxidation.[29–33] Photocatalytic degradation is a very attractive approach, particularly if it can be accomplished with the use of visible light.[34] Different types of materials are being investigated for this purpose.[35] Among the most studied materials are inorganic semiconductors such as titanium and zinc oxides (TiO_2 and ZnO), which, due to their powerful oxidation capability, have been successfully used in organic,[36]

Materials Science Institute of Madrid – Spanish National Research Council (ICMM-CSIC), C/Sor Juana Inés de la Cruz 3, 28049, Madrid, Spain.
E-mail: egutierrez@icmm.csic.es, gandara@icmm.csic.es

† Electronic supplementary information (ESI) available: Experimental details. See DOI: https://doi.org/10.1039/d4lf00233d

‡ Present address: Department of Materials Science and Metallurgy, University of Cambridge, 27 Charles Babbage Road, CB30FS, Cambridge, United Kingdom.

inorganic[37] and pathogenic[38,39] pollutant degradation processes. Other semiconductors with band gaps of less than 3 eV have also been used as photocatalysts for pollutant degradation.[40,41] Among photocatalysts whose activity has been studied and shown favourable results are nanomaterials doped with different metals, successfully used in water remediation processes,[42–44] and composites formed from different semiconductors, which show an improvement of photocatalytic activity for pollutant degradation compared to isolated semiconductors.[45,46] To improve photocatalyst recyclability and recovery in water decontamination processes, immobilised photocatalysts have been extensively studied in the last few years.[47,48] Carbon-based nanomaterials,[49,50] glass,[51,52] clays,[53,54] polymers[55,56] and zeolites[57] have been studied as substrates or support materials for these processes.

Following, we have investigated MM-MTV-MOFs comprising combinations of up to four different metal elements as precursors to generate complex solids with photocatalytic activity in the degradation of pollutants. Particularly, we have employed MOFs with various combinations of zinc, cobalt, calcium and manganese to generate new metal–organic derived ensembles (MODEs) through a pyrolysis process. The resulting materials have been characterized using a combination of techniques showing that each one of the different metal elements initially incorporated in the MOF atomic sequence affords a different chemical component in the resulting MODE (Scheme 1). We show that they are effective photocatalysts for the degradation of organic dyes under visible light irradiation, and one of the studied materials is also active in the photodegradation of paracetamol.

Results and discussion

To synthesize new metal–organic derived ensembles, various isoreticular ZnMnCoCa MOFs were synthesized by previously reported solvothermal methods.[58] In a typical synthesis, the organic linker 4,4′-(hexafluoroisopropylidene)bis(benzoic acid) (H_2hfipbb) and the selected metal elements were mixed and dissolved in a mixture of 10 mL of water, 10 mL of ethanol, and 0.6 mL of 1 M HNO_3, keeping a linker to metal ratio of 1 : 1.65. The mixtures were heated at 170 °C for an overnight period, and the resulting solids were filtered and washed with water and ethanol. For the MOF synthesis, we chose initial Zn : Mn : Co : Ca metal ratios of 1 : 1 : 1 : 7, 1 : 4 : 4 : 1 and 2 : 1 : 2 : 2, which afforded compounds with compositions $Zn_{0.37}Mn_{0.28}Co_{0.13}Ca_{0.22}$(hfipbb), $Zn_{0.16}Mn_{0.47}Co_{0.33}Ca_{0.03}$(hfipbb), and $Zn_{0.46}Mn_{0.21}Co_{0.17}Ca_{0.15}$(hfipbb), respectively, as determined by ICP-MS analysis (see S1† for details). We chose these initial ratios, as they were previously proved to generate highly active multimetal oxides.

Their corresponding MODEs (Scheme 1, right) were obtained from a pyrolysis process by heating the selected MOF precursor in a furnace under a N_2 flow in two steps, first from room temperature to 80 °C with a heating rate of 0.3 °C min^{-1}, and then from 80 °C to 700 °C with a heating rate of 5 °C min^{-1}. Once this temperature was reached, the samples were kept at 700 °C for 4 h, and then cooled down to room temperature. The resulting solids, which are herein labelled with the number corresponding to the molar ratio employed for the synthesis of their MOF precursors, were characterized by means of powder X-ray diffraction (PXRD), scanning electron microscopy (SEM) and transmission electron microscopy (TEM).

The experimental PXRD patterns for the samples are consistent with the presence of metallic cobalt and MnF_2 as the only detectable crystalline phases (Fig. 1). Previously, we observed that under a reducing environment, such as a hydrogen atmosphere and high temperature (700 °C), cobalt atoms present in metal–organic derived oxides (MODOs) are reduced and form metal nanoparticles. In the present case, metallic cobalt is formed directly from the heating of the

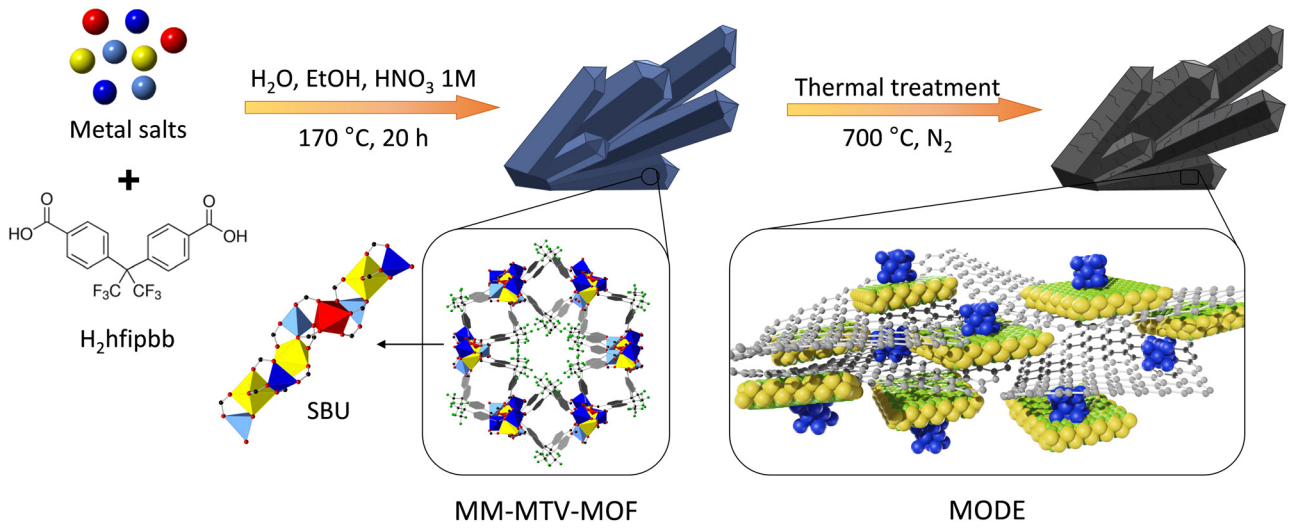

Scheme 1 Different metal elements are arranged in the secondary building unit of MOFs and subsequently pyrolyzed to produce metal–organic derived ensembles.

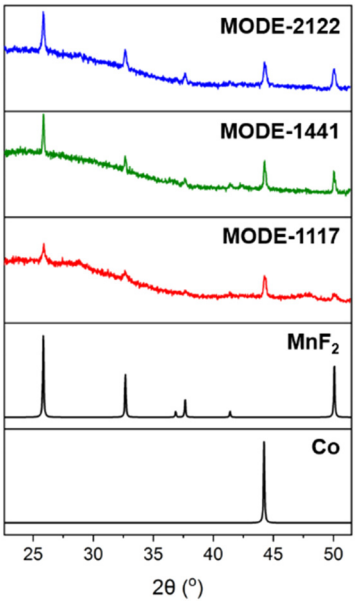

Fig. 1 Comparison of the experimental PXRD patterns for MODEs-2122 (blue), -1441 (green), and -1117 (red) with the calculated PXRD patterns (black) for MnF_2 (PDF 01-083-2417) and Co (PDF 00-015-0806).

MOF under a nitrogen atmosphere, with a reducing environment that is likely provided by the simultaneous decomposition of the organic linker, as previously observed with other MOFs,[59] which in addition provides the fluorine atoms for the formation of manganese fluoride.

Scanning electron microscopy (SEM) images show that the morphology of the MOF precursor particles (Fig. S1†) is generally preserved after the pyrolysis process, as shown in Fig. 2 where the SEM images of the prepared MODEs are displayed. In the case of MODE-1441, the particles are formed by aggregates, which are clearly visible on the surface.

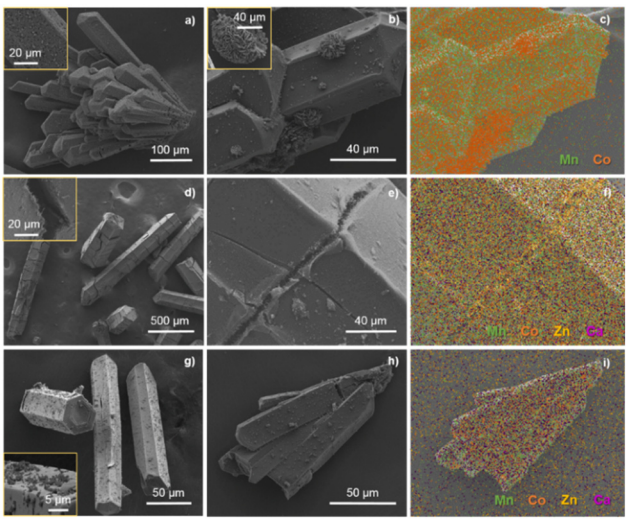

Fig. 2 SEM images of the MODEs (a and b) 1441, (d and e) 1117, and (g and h) 2122, and the EDX mapping of the pyrolyzed derived composite crystals for MODEs (c) 1441, (f) 1117 and (i) 2122. Insets show zoomed areas.

For the remaining MODE combinations, the metal distribution is more uniform along the surface, with only minor aggregates observed for Co in MODE-2122 (Fig. 2, right). The energy dispersive X-ray spectroscopy (EDX) study (Fig. 2c) revealed that in all cases, carbon is clearly present on the particle surfaces. As for the presence of the different metal elements, these appear with varying distributions for each material, illustrating the influence of the initial distribution in the MOF on the resulting MODE. Thus, in the case of MODE-1441, elemental mapping shows areas with higher concentrations of cobalt, while manganese is more evenly distributed. Signals for zinc and calcium only appear as background noise, which is consistent with the point EDX measurements carried out for this sample that did not show the presence of these elements (Fig. S2†). The absence of zinc is consistent with the low melting point of this element (419.5 °C), indicating that it is mostly carried away during the pyrolysis process.[60] Nevertheless, the use of zinc is required as a structure directing element for the preparation of the MOFs.[58] The use of calcium is motivated by its previously demonstrated beneficial role in activity;[15] however, the small initial amount of this element results in the impossibility to detect it within the surfaces (Fig. S3†).

In contrast, the elemental mapping of MODE-1117, which is obtained from a MOF with a much higher amount of calcium, shows the clear presence of this element (Fig. S5†). Moreover, calcium is found to be distributed similarly to manganese and fluoride and no particular area of high calcium concentration is visible in the EDX maps, suggesting that it is incorporated now in the same manganese fluoride structure that was identified with PXRD. Cobalt is found to be evenly distributed along the entire MODE. Interestingly, zinc is now also detected on the particle surfaces, particularly concentrated in areas where the MOF crystals are cracked, and small (sub-micron) needles are observed (Fig. 2e, f and S4†).

Finally, elemental mapping of MODE-2122 shows the absence of zinc on the surfaces, but the presence of calcium, although in a significantly smaller amount, but distributed along the entire MODE. Cobalt is specifically found on visible small surface particles, whereas Mn distribution follows Ca and F (Fig. S6 and S7†).

To further investigate the different components in one of the MODE materials, a transmission electron microscopy (TEM) analysis was carried out. For this, the particles of MODE-1441 were first dispersed with the help of ultrasound. The TEM images show the presence of two types of particles with different sizes, supported on a visible carbonaceous matrix (Fig. 3a and b and S8–S10†). The EDX mapping of a sample region clearly shows that cobalt and manganese are segregated in different particles, with some of them being mostly composed of manganese and fluoride, while others are made of just cobalt (Fig. 3c–f, S11 and S12†). The combined results of the PXRD, SEM, TEM and EDX analyses confirm that the MODEs resulting from the pyrolysis process are formed by cobalt nanoparticles

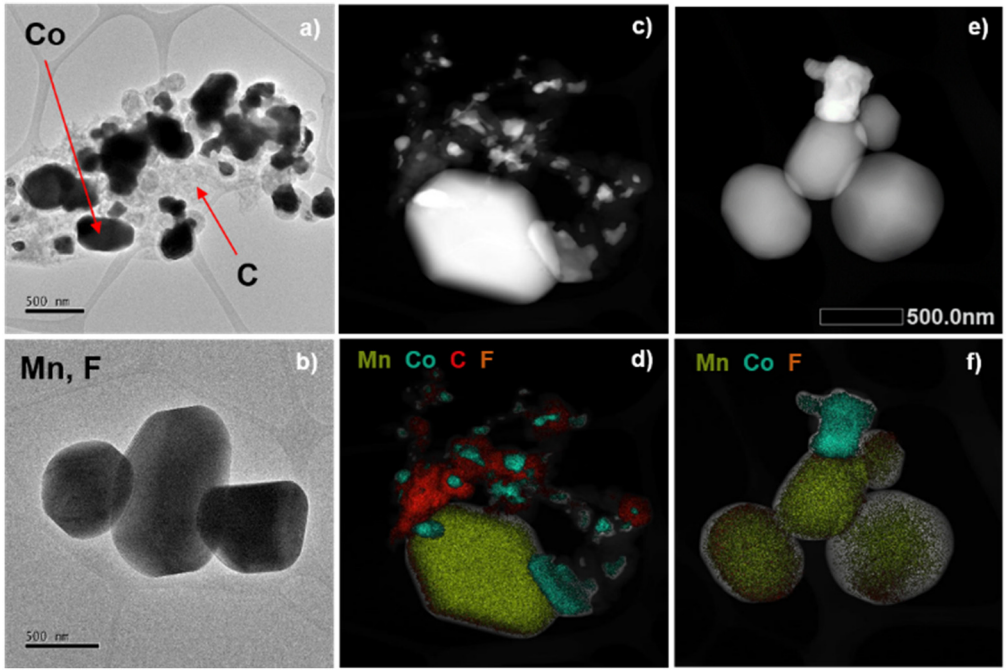

Fig. 3 TEM images (a and b) and mapping (c–f) of the MODE-1441 crystals.

supported on manganese fluoride and embedded in a carbonaceous matrix. For samples obtained from MOFs with a larger amount of calcium, this element is incorporated into the MnF_2 particles, whereas zinc is typically lost as a volatile species during the pyrolysis process, and thus it is not observed in the MODEs.

Photocatalytic activity studies

The ability of MODEs as photocatalysts was evaluated by UV-visible spectroscopy (290–800 nm) in the degradation of two organic dyes namely methyl orange (MO) and methyl red (MR). Experiments were carried out in a closed reactor, into which a radiation source (blue light, λ = 440 nm) was introduced together with the vials arranged in an adapter holder (see S3.1† for details). The MODE samples (5 mg) were stirred in 5 mL of a 10 ppm dye solution under an O_2 atmosphere at room temperature, whereupon they were separated by centrifugation and the UV-vis absorption spectrum of the resulting solution was measured. Fig. 4 shows the absorption spectra for the MO solutions after 18 h reaction in the presence of the three MODEs. Blank experiments indicate that no photodegradation occurs under an air or O_2 atmosphere in the absence of any catalyst. The spectra show significant differences in the activity of MODE-1117, which only achieves 9% degradation, while MODE-1441 and MODE-2122 reach 100% degradation. In the case of MODE-2122, 58% and 85% degradation rates are achieved after only 1 and 5 h, respectively (Fig. S14†).

Considering that the main observed difference among the three MODEs during the SEM study was that the presence of Co particles aggregated with MnF_2 particles was visible for MODE-1441 and MODE-2122, but not for MODE-1117, it is reasonable to think that this combination has a major influence on the photodegradation activity for MO.

The synergetic effect offered by the multiple components present in the MODEs is further demonstrated by the fact that the MOF precursor (1441) did not show any degradation ability (Fig. S15†). Conversely, other MOF derived oxides with various compositions were also tested, equally showing nearly null photodegradation activity (Fig. S17†), further demonstrating that the supported particles conforming the MODEs are the active species for this process.

To investigate the capability to degrade other contaminants, we also tested the activity of MODE-1441 and MODE-1117 in the photodegradation of another dye (methyl

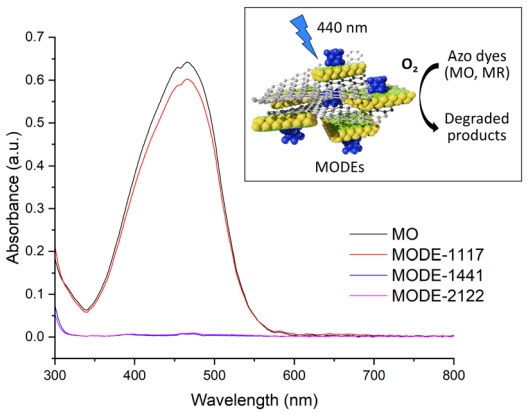

Fig. 4 Comparative UV-vis spectra of methyl orange (black), after 18 h under blue light irradiation and an O_2 atmosphere, with MODE-1117 (red), MODE-1441 (blue) and MODE-2122 (pink). Inset: Scheme of the photooxidative degradation process for MO and MR using MODEs.

red) as well as in the photodegradation of the drug paracetamol. In the case of MR, using the same light source and O_2 atmosphere, 100% and 72% photodegradation was achieved after 18 h for MODE-1441 and MODE-1117, respectively (Fig. S16†).

Paracetamol (PMA) photodegradation studies were performed following a similar procedure, but under a violet light ring as a radiation source (λ = 405 nm), under an air atmosphere and with a reaction time of 18 hours. For all tests, 4 mL of a 1000 ppm paracetamol solution was used. Paracetamol quantification after the photocatalytic reaction was monitored by means of chromatographic techniques, specifically HPLC combined with UV-vis detection. A solution of naphthol (Nph) (10 000 ppm) was used as a reference. The HPLC conditions used for all measurements were as follows: flow rate 0.7 mL min^{-1}, mobile phase distilled water : acetonitrile (80 : 20) and wavelength 297 nm. For reference conditions, paracetamol and naphthol signals appear at 2.992 min and 2.835 min, respectively. A PMA : Nph mixture was used to obtain the calibration curve for the paracetamol concentration, using PMA standards in concentrations between 0 and 1000 ppm and a fixed Nph 10 000 ppm volume. To determine the PMA concentration, the area ratio between Nph and NPh + PMA was measured. The obtained data fit the equation:

$$A_{Nph}/A_{PMA} = 0.34 + 6.46 \times e^{(-C_{PMA}/132.5)}$$ (Fig. S18†)

In previous studies of paracetamol degradation, sulphuric acid was used to adjust the pH of the medium,[61] so the studies were carried out in the presence and absence of the acid. It was observed that under the above-mentioned reaction conditions and in the absence of a catalyst, a 1000 ppm paracetamol solution was degraded by 7.7%, and by 16.3% with the addition of 100 μl H_2SO_4. In the presence of MODE-1441 and under the same conditions, the paracetamol degradation rate amounted to 26.9% in the absence of the acid, and up to 45.9% by adding 100 μl of H_2SO_4 (pH = 3), indicating a three-fold increase in the degradation rate thanks to the activity of the catalyst and demonstrating the potential use of the material under harsh conditions (see S3.3† for details).

Conclusions

In summary, we have reported here the preparation and characterization of three new materials obtained through the pyrolysis process of multi-metal MOFs. The resulting metal–organic derived ensembles, MODEs, are demonstrated to be formed by a carbonaceous matrix, with embedded manganese fluoride particles that contain cobalt nanoparticles on their surface. These materials are demonstrated to be highly active in the photodegradation processes of water contaminants such as organic dyes or paracetamol, thanks to the synergetic activity of the different chemical components.

In light of these results, the present study provides additional evidence of the potential applications of complex systems derived from multi-metal MOFs, thereby encouraging further research on the correlation between the composition of the initial MOF and the final composition in its complex derived systems. This may facilitate the development of MOF-derived ensembles with optimized ratios for a range of applications.

Data availability

The data supporting this article have been included as part of the ESI.†

Author contributions

Conceptualization: MAM, EGP, and FG; formal analysis: CLG, MI, MAM, EGP, and FG; funding acquisition: MI, EGP, MAM, and FG; investigation: CLG and CCB; writing – original draft: CLG and FG; writing – review & editing: all authors.

Conflicts of interest

There are no conflicts to declare.

Acknowledgements

This work has received financial support through projects PID2021-123287OB-I00, PID2020-112590GB-C22, and PID2019-107675RB-100, funded by MCIN/AEI/10.13039/501100011033 and ERDF A way to make Europe, and PLEC2021-007906 (SOLFuture) funded by MCIN/AEI/10.13039/501100011033 and European Union NextGenerationEU/PRTR.

Notes and references

1 H. Furukawa, K. E. Cordova, M. O'Keeffe and O. M. Yaghi, *Science*, 2013, **341**, 1230444.
2 L. Chen, H.-F. Wang, C. Li and Q. Xu, *Chem. Sci.*, 2020, **11**, 5369–5403.
3 J. Castells-Gil, N. Almora-Barrios, B. Lerma-Berlanga, N. M. Padial and C. Martí-Gastaldo, *Chem. Sci.*, 2023, **14**, 6826–6840.
4 S. Wang, W. Xu and W. Ma, *Mater. Lett.*, 2024, **362**, 136205.
5 P. Duan, H. Wang, H. Zhou, S. Zhang, X. Meng, Q. Duan, K. Jin and J. Sun, *J. Colloid Interface Sci.*, 2024, **660**, 974–988.
6 G. Asghar, M. Fiaz, M. A. Farid, M. N. Ashiq and M. Athar, *Int. J. Hydrogen Energy*, 2024, **51**, 1435–1447.
7 T. Wu, F. Ren, Z. Guo, J. Zhang, X. Hou, Z. Chen, Y. Jin and P. Ren, *J. Alloys Compd.*, 2024, **976**, 172984.
8 D. Huang, G. Wang, M. Cheng, G. Zhang, S. Chen, Y. Liu, Z. Li, W. Xue, L. Lei and R. Xiao, *Chem. Eng. J.*, 2021, **421**, 127817.
9 S.-R. Zhu, M.-K. Wu, W.-N. Zhao, F.-Y. Yi, K. Tao and L. Han, *J. Solid State Chem.*, 2017, **255**, 17–26.

10 J.-L. Niu, H.-J. Peng, C.-H. Zeng, X.-M. Lin, P. Sathishkumar, Y.-P. Cai and A.-W. Xu, *Chem. Eng. J.*, 2018, **336**, 510–517.
11 X. Zhang, S. Xiang, Q. Du, F. Bi, K. Xie and L. Wang, *Mol. Catal.*, 2022, **522**, 112226.
12 Y. Hao, G. Du, Y. Fan, L. Jia, D. Han, W. Zhao, Q. Su and B. Xu, *Appl. Surf. Sci.*, 2023, **614**, 156237.
13 N. Sun, L. Wang, Y. Zhang, Z. Cao and J. Sun, *ACS Appl. Nano Mater.*, 2023, **6**, 18823–18836.
14 C. Castillo-Blas, N. López-Salas, M. C. Gutiérrez, I. Puente-Orench, E. Gutiérrez-Puebla, M. L. Ferrer, M. Á. Monge and F. Gándara, *J. Am. Chem. Soc.*, 2019, **141**, 1766–1774.
15 C. Castillo-Blas, C. Álvarez-Galván, I. Puente-Orench, A. García-Sánchez, F. E. Oropeza, E. Gutiérrez-Puebla, Á. Monge, V. A. de la Peña-O'Shea and F. Gándara, *Nano Res.*, 2021, **14**, 493–500.
16 Z. Lu, L. Guo, Q. Shen, F. Bi, C. Li and X. Zhang, *Sep. Purif. Technol.*, 2024, **340**, 126772.
17 S. Ren, P. Mo, A. Shui, J. Qian and B. Du, *J. Mater. Sci.: Mater. Electron.*, 2024, **35**, 530.
18 X. Chen, M. X. Li, J. L. Yan and L. L. Zhang, *Xinxing Tan Cailiao*, 2024, **39**, 78–99.
19 F. Wang, Y. Gao, S.-S. Liu, X.-H. Yi, C.-C. Wang and H. Fu, *Chem. Eng. J.*, 2023, **463**, 142466.
20 J. Xu, J. Gao, Y. Liu, Q. Li and L. Wang, *Mater. Res. Bull.*, 2017, **91**, 1–8.
21 S.-W. Lv, J.-M. Liu, N. Zhao, C.-Y. Li, F.-E. Yang, Z.-H. Wang and S. Wang, *Sep. Purif. Technol.*, 2020, **253**, 117413.
22 Y. Wang, X. Liu, L. Guo, L. Shang, S. Ge, G. Song, N. Naik, Q. Shao, J. Lin and Z. Guo, *J. Colloid Interface Sci.*, 2021, **599**, 566–576.
23 L. Yu, Y. Zhao, S. Guo and J. Xue, *Catal. Lett.*, 2024, DOI: **10.1007/s10562-024-04654-6**.
24 T. Jiang, X. Wang, J. Zhang, Y. Mai and J. Chen, *Microporous Mesoporous Mater.*, 2024, **368**, 113035.
25 W. L. Ma, Y. Q. Zhang, W. Z. Li, J. Li and J. Luan, *Dalton Trans.*, 2024, **53**, 4314–4324.
26 W. Ji, W. Li, Y. Wang, T. C. Zhang and S. Yuan, *Sep. Purif. Technol.*, 2024, **334**, 126003.
27 Y. Li, D. Ren, S. Guo, M. Wang, J. Zhai, S. Zhang, X. Gong and X. Zhang, *J. Mol. Struct.*, 2024, **1299**, 137058.
28 L. Zhang, J. Chen, L. B. Song, J. J. Pan and Q. Luo, *Prog. Nat. Sci.: Mater. Int.*, 2023, **33**, 544–550.
29 F. Yu, X. Bai, M. Liang and J. Ma, *Chem. Eng. J.*, 2021, **405**, 126960.
30 G. Zhu, Y. Bian, A. S. Hursthouse, S. Xu, N. Xiong and P. Wan, *Chemosphere*, 2020, **247**, 125921.
31 X. Yin, S. Tang, Q. Yong, X. Zhang and J. M. Catchmark, *Sep. Purif. Technol.*, 2021, **276**, 119366.
32 Z. A. Stoll, C. Forrestal, Z. J. Ren and P. Xu, *J. Hazard. Mater.*, 2015, **283**, 847–855.
33 J. Liu, L. Zhao, H. Geng, B. Wang, X. Tong, Y. Li, D. Chen, P. Sun and Y. Yang, *J. Environ. Chem. Eng.*, 2023, **11**, 110649.
34 A. J. Chacón-García, S. Rojas, E. S. Grape, F. Salles, T. Willhammar, A. K. Inge, Y. Pérez and P. Horcajada, *Sci. Rep.*, 2024, **14**, 7882.
35 V. K. Parida, S. K. Srivastava, A. K. Gupta and A. Rawat, *Mater. Express*, 2023, **13**, 1–38.
36 X. Chen, Z. Wu, D. Liu and Z. Gao, *Nanoscale Res. Lett.*, 2017, **12**, 143.
37 Z. Wei, Y. Fang, Z. Wang, Y. Liu, Y. Wu, K. Liang, J. Yan, Z. Pan and G. Hu, *Chemosphere*, 2019, **225**, 434–442.
38 C.-Y. Chen, L.-C. Wu, H.-Y. Chen and Y.-C. Chung, *Water, Air, Soil Pollut.*, 2010, **212**, 231–238.
39 J. Lee, K. Zoh and G. Ko, *Appl. Environ. Microbiol.*, 2008, **74**, 2111–2117.
40 T. O. Ajiboye, O. A. Oyewo and D. C. Onwudiwe, *Surf. Interfaces*, 2021, **23**, 100927.
41 Q. Zheng, D. P. Durkin, J. E. Elenewski, Y. Sun, N. A. Banek, L. Hua, H. Chen, M. J. Wagner, W. Zhang and D. Shuai, *Environ. Sci. Technol.*, 2016, **50**, 12938–12948.
42 G. Palani, R. Apsari, M. M. Hanafiah, K. Venkateswarlu, S. K. Lakkaboyana, K. Kannan, A. T. Shivanna, A. M. Idris and C. H. Yadav, *Nanomaterials*, 2022, **12**, 1754.
43 C. Adán, A. Bahamonde, I. Oller, S. Malato and A. Martínez-Arias, *Appl. Catal., B*, 2014, **144**, 269–276.
44 Y. An, D. J. de Ridder, C. Zhao, K. Schoutteten, J. Vanden Bussche, H. Zheng, G. Chen and L. Vanhaecke, *Water Sci. Technol.*, 2016, **73**, 2868–2881.
45 N. Li, J. Zhang, Y. Tian, J. Zhao, J. Zhang and W. Zuo, *Chem. Eng. J.*, 2017, **308**, 377–385.
46 C. Belver, J. Bedia, M. Peñas-Garzón, V. Muelas-Ramos, A. Gómez-Avilés and J. J. Rodriguez, in *Visible Light Active Structured Photocatalysts for the Removal of Emerging Contaminants*, Elsevier, 2020, pp. 41–98.
47 H. Chawla, S. Garg, P. P. Ingole and A. Chandra, in *Green Photocatalytic Semiconductors*, Springer US, 2022, pp. 445–473.
48 V. Parvulescu, M. Ciobanu and G. Petcu, in *Handbook of Smart Photocatalytic Materials*, Elsevier, 2020, pp. 103–140.
49 T. V. H. Luu, M. D. Luu, N. N. Dao, V. T. Le, H. T. Nguyen and V. D. Doan, *J. Dispersion Sci. Technol.*, 2021, **42**, 1311–1322.
50 W. Liu, Y. Li, F. Liu, W. Jiang, D. Zhang and J. Liang, *Water Res.*, 2019, **151**, 8–19.
51 A. Akbari Shorgoli and M. Shokri, *Chem. Eng. Commun.*, 2017, **204**, 1061–1069.
52 V. Vaiano and G. Iervolino, *J. Colloid Interface Sci.*, 2018, **518**, 192–199.
53 E. Hass Caetano Lacerda, F. C. Monteiro, J. R. Kloss and S. T. Fujiwara, *J. Photochem. Photobiol., A*, 2020, **388**, 112084.
54 E. Magnone, M. K. Kim, H. J. Lee and J. H. Park, *Ceram. Int.*, 2021, **47**, 7764–7775.
55 H. S. Zakria, M. H. D. Othman, R. Kamaludin, S. H. Sheikh Abdul Kadir, T. A. Kurniawan and A. Jilani, *RSC Adv.*, 2021, **11**, 6985–7014.
56 F. Gao, X. Hou, A. Wang, G. Chu, W. Wu, J. Chen and H. Zou, *Particuology*, 2016, **26**, 73–78.

57 J. Liu, H. Lin, Y. Dong, Y. He and C. Liu, *Chemosphere*, 2022, **287**, 132211.
58 C. Castillo-Blas, V. A. De La Peña-O'Shea, I. Puente-Orench, J. R. De Paz, R. Sáez-Puche, E. Gutiérrez-Puebla, F. Gándara and Á. Monge, *Sci. Adv.*, 2017, **3**, 1–11.
59 Y. Wu, Z. Huang, H. Jiang, C. Wang, Y. Zhou, W. Shen, H. Xu and H. Deng, *ACS Appl. Mater. Interfaces*, 2019, **11**, 44573–44581.
60 P. Yin, T. Yao, Y. Wu, L. Zheng, Y. Lin, W. Liu, H. Ju, J. Zhu, X. Hong, Z. Deng, G. Zhou, S. Wei and Y. Li, *Angew. Chem., Int. Ed.*, 2016, **55**, 10800–10805.
61 G. E. do Nascimento, M. A. Soares Oliveira, R. M. da Rocha Santana, B. G. Ribeiro, D. C. Silva Sales, J. M. Rodríguez-Díaz, D. C. Napoleão, M. A. da Motta Sobrinho and M. M. M. B. Duarte, *Water Sci. Technol.*, 2020, **81**, 2545–2558.